



Water Resources Research

RESEARCH ARTICLE

10.1029/2020WR027873

Key Points:

- We use synchrotron X-ray microtomography to quantify dynamics of three-phase flow and trapping in porous media
- The wettability order for immiscible three-phase flow in a mixed-wet rock was oil-water-gas from the most to the least wetting phase
- Oil flow and gas trapping were measured using topological descriptors and were found to be both favored by the wettability alteration

Correspondence to:

A. Scanziani,
alessio.scanziani16@imperial.ac.uk

Citation:

Scanziani, A., Alhosani, A., Lin, Q., Spurin, C., Garfi, G., Blunt, M. J., & Bijeljic, B. (2020). In situ characterization of three-phase flow in mixed-wet porous media using synchrotron imaging. *Water Resources Research*, 56, e2020WR027873. <https://doi.org/10.1029/2020WR027873>

Received 17 MAY 2020

Accepted 1 AUG 2020

Accepted article online 11 AUG 2020

In Situ Characterization of Three-Phase Flow in Mixed-Wet Porous Media Using Synchrotron Imaging

Alessio Scanziani¹ , Abdulla Alhosani¹, Qingyang Lin¹ , Catherine Spurin¹ , Gaetano Garfi¹ , Martin J. Blunt¹ , and Branko Bijeljic¹ 

¹Department of Earth Science and Engineering, Imperial College London, London, UK

Abstract We use fast synchrotron X-ray microtomography to understand three-phase flow in mixed-wet porous media to design either enhanced permeability or capillary trapping. The dynamics of these phenomena are of key importance in subsurface hydrology, carbon dioxide storage, oil recovery, food and drug manufacturing, and chemical reactors. We study the dynamics of a water-gas-water injection sequence in a mixed-wet carbonate rock. During the initial waterflooding, water displaced oil from pores of all size, indicating a mixed-wet system with local contact angles both above and below 90°. When gas was injected, gas displaced oil preferentially with negligible displacement of water. This behavior is explained in terms of the gas pressure needed for invasion. Overall, gas behaved as the most nonwetting phase with oil as the most wetting phase; however, pores of all size were occupied by oil, water, and gas, as a signature of mixed-wet media. Thick oil wetting layers were observed, which increased oil connectivity and facilitated its flow during gas injection. A chase waterflooding resulted in additional oil flow, while gas was trapped by oil and water. Furthermore, we quantified the evolution of the surface areas and both Gaussian and the total curvature, from which capillary pressure could be estimated. These quantities are related to the Minkowski functionals which quantify the degree of connectivity and trapping. The combination of water and gas injection, under mixed-wet immiscible conditions, leads to both favorable oil flow and significant trapping of gas, which is advantageous for storage applications.

1. Introduction

Three-phase flow in porous media is observed in many natural and engineered processes. These include nonaqueous phase liquid (NAPL) contaminant removal, gas storage in oil reservoirs, and enhanced oil recovery (EOR) (Scanziani et al., 2018). EOR can be combined with gas storage, for example, when storing CO₂ underground to mitigate climate change (carbon capture and storage, CCS) (Szulczewski et al., 2012). In this case, it would be ideal if high oil recovery is combined with significant gas storage (Ampomah et al., 2017; Scanziani, Singh, et al., 2020). Since depleted hydrocarbon fields contain injection infrastructure, CCS is an attractive option with the potential economic benefit of additional oil recovery: Combining CCS with EOR could be a key technology to enable storage at the gigatonne scale necessary to make a significant impact on preventing dangerous climate change (Bellamy & Geden, 2019; Bickle, 2009; Scott et al., 2015).

The flow of three fluid phases—two liquid phases and one gaseous phase—is also important in many manufacturing contexts, to synthesize emulsions containing droplets and microbubbles, for food manufacture (Zúñiga & Aguilera, 2008), drug delivery (Ferrara et al., 2009), and the synthesis of microcapsules (Chen et al., 2019). Microfluidics devices can be designed to form porous media of desired structure and composition, controlled by the interaction of wettability, flow, and pore space topology. Three-phase flow is also encountered in packed bed reactors and catalysis with applications in biological waste water treatment and fluid separation, for instance (Kundu et al., 2008).

The optimization of these processes can be achieved only with an accurate study of the flow and trapping of the three phases, bearing in mind that the physics controlling the flow are defined at the micron scale of the pore space (Blunt, 2017). Previous studies have used micromodels to investigate three-phase flow in porous media at the pore scale. Øren et al. (1992) visualized the formation of spreading oil layers, in a quasi 2-D water-wet micromodel. The formation of spreading layers around droplets has also been

©2020. The Authors.

This is an open access article under the terms of the Creative Commons Attribution License, which permits use, distribution and reproduction in any medium, provided the original work is properly cited.

observed in microfluidics devices (Chen et al., 2019). Other studies have identified the occurrence of multiple displacements (when one phase displaces another which in turn displaces the third one) in micromodels with variable wettability (Sohrabi et al., 2008; Van Dijke et al., 2006).

However, the use of micromodels may not capture the intricate behavior of multiphase flow in the complex pore space of 3-D porous media which include rocks, soils, and catalysts. Advances in both X-ray imaging and associated analysis methods, which allow direct *in situ* visualization of the pore space and the fluids within it, have revolutionized our understanding of flow in porous media (Bultreys et al., 2016; Pak et al., 2015; Wildenschild & Sheppard, 2013). Previous work on two-phase (oil and water or CO₂ and water) flow with application to improved carbon dioxide storage and oil recovery highlighted the crucial role of wettability as a determinant of flow behavior, trapping, and recovery (Alhammadi et al., 2020; AlRatrou et al., 2018; Qin et al., 2019). In particular, mixed-wettability—where the solid surface has regions that are both water-wet and oil-wet, indicating contact angles between oil and water both above and below 90°—leads to well-connected oil and water phases and favorable oil recovery (Kovscek et al., 1993; Morrow, 1990; Scanziani, Lin, et al., 2020). The fluid-fluid interfaces have almost zero mean curvature, with approximately equal but opposite principal curvatures in orthogonal directions, forming minimal surfaces (Lin, Bijeljic, Berg, et al., 2019).

However, further complexities arise in three-phase flow, where the interaction among three phases at their interface strongly influences multiphase flow phenomena and eventually oil flow and gas trapping. The spreading coefficient of a phase *i*, C_{si} , defines if the phase *i* is allowed to form spreading layers sandwiched between the other two (Feali et al., 2012; Hirasaki, 1993). The formation of these layers is favored if $C_{si} \approx 0$ (Adamson & Gast, 1997). In this study, we will employ fast synchrotron X-ray microtomography to examine the dynamics of layer formation in mixed-wet media.

One principal characteristic of three-phase flow, which will be the emphasis of this paper, is the wettability order according to which different phases arrange in pore space (Piri & Blunt, 2005; Van Dijke & Sorbie, 2002). The wettability of a phase with respect to another is directly defined by the contact angle θ at their interface (Andrew et al., 2014; Blunt, 2017; Scanziani et al., 2017). The wettability order defines which phase more favorably wets the surface of the rock and which one instead preferentially resides in the center of the pores (Van Dijke & Sorbie, 2002). This arrangement of the phases in the pore space has consequences on their flow and hence the relative permeability of each phase (Alizadeh & Piri, 2014; Fenwick & Blunt, 1998; Hui & Blunt, 2000). Pore occupancy, defined as a relation between the dimension of the pores and the phase which occupies them, can be provided by X-ray microtomography and used to identify the wettability order in three-phase flow (Alhosani et al., 2019; Bultreys et al., 2018; Scanziani et al., 2018). The phase which occupies the smallest pores is the most wetting phase, while the least wetting phase preferentially occupies the largest pores. The most nonwetting phase has the largest flow potential while it is connected but can also be trapped by the other phases, adding to storage security, for instance.

In three-phase flow, *in situ* pore-scale imaging studies have been concerned, to date, principally with water-wet media (Alizadeh & Piri, 2014; Brown et al., 2014). In this case, the wettability order is water-oil-gas from most to least wetting (Alhosani et al., 2019; Khishvand et al., 2016; Scanziani et al., 2018). In water-wet media, as previously observed in micromodels (Feali et al., 2012; Øren et al., 1992) and porous rocks (Scanziani et al., 2018), oil can form spreading layers sandwiched between water that wets the surface and gas that preferentially fills the larger pores. Gas can become trapped by both oil and water. Indeed, since spreading oil layers can completely wet the gas, the trapping of gas can be enhanced compared to two-phase gas-water displacement, which provides a rapid and secure mechanism to retain gas in the subsurface for storage (Amaechi et al., 2014; Scanziani, Singh, et al., 2020). Even if the majority of oil fields are not water-wet, only a few studies have investigated the effect of wettability alteration on three-phase flow. Qin et al. (2019) studied gas and water injection in a weakly oil-wet carbonate. They observed favorable oil recovery by gas injection as a result of gas-oil-water double displacement processes, with further recovery combined with gas trapping after subsequent waterflooding. They studied the static arrangement of the phases at the end of each injection. However, the evolution of the pore-scale arrangement of the phases during a displacement was not studied.

The use of bright X-rays at synchrotron sources allows for images to be taken with a time resolution of approximately 1 min, and hence it is a powerful technique to study the dynamics of multiphase flow (Armstrong & Berg, 2013; Berg et al., 2013; Wildenschild et al., 2005). In particular, it has the capability

to visualize and quantify how displacement proceeds on a pore-by-pore basis providing great insight into two-phase flow processes (Andrew et al., 2015; Reynolds et al., 2017; Singh et al., 2017). We will extend the use of synchrotron imaging to the simultaneous flow of three phases in mixed-wet media.

Advances in visualization have been complemented by analysis methods derived from algebraic topology (Armstrong et al., 2019). Specifically, the measurement of Minkowski functionals links the geometry and topology of pore space with physical quantities, such as the connectivity of the fluid phases (Liu et al., 2017; Mecke & Stoyan, 2000). Considering a solid in Euclidean 3-D space, four Minkowski functionals are defined: volume, surface area, total curvature, and Gaussian curvature (Vogel et al., 2010). We will use this set of measures to provide a complete characterization of the phases within the pore space, relating the topological information with physical characteristics of the flow and trapping such as saturations, capillary pressure, and connectivity.

The main objective of this study is to understand the dynamics of three-phase flow in mixed-wet porous media and how this is controlled by the wettability order. To this end, we employ fast synchrotron tomography to study gas injection followed by water injection in a mixed-wet carbonate sample. Scanziani, Singh, et al. (2020) performed synchrotron experiments of three-phase flow on a similar carbonate rock under water-wet conditions, observing the dynamics of the formation of spreading oil layers and the double capillary trapping of gas.

In section 2, we describe the materials of the experiment and the methods that we used to dynamically image three-phase flow in a mixed-wet carbonate rock and analyze the resulting 3-D images of the three phases flowing inside the pore space.

As we seek to understand the key determinants governing displacement, in section 3.1, we discuss the assessment of the wettability of the sample using contact angle measurements, pore occupancy, surface area coverage, and visual inspection. In section 3.2, we describe the dynamics of gas injection and second waterflooding, and in the next sections, we detail the formation of oil layers (section 3.3) and gas trapping (section 3.4) and their effect on oil flow and gas storage.

We compare and discuss our results in the light of previous measurements made on a similar water-wet system (Scanziani et al., 2018; Scanziani, Singh, et al., 2020) and the same rock under near-miscible conditions (Alhosani et al., 2019) using the Minkowski functionals to quantify our observations (section 3.5). Finally, we will place our work in context by exploring the implications for storage, recovery, and the performance optimization of manufactured porous devices.

2. Materials and Methods

We used a cylindrical sample of Ketton limestone, with a length of 16.1 mm and a diameter of 5.8 mm. The total porosity was measured to be 28.3% with a Helium porosimeter, while the apparent porosity obtained with image processing was 14.3%. This latter value represents the porosity of the macropores resolvable in the image; the oolithic grains of the rock are also porous, but these micropores cannot be explicitly seen in the images. The pore volume (PV) of the sample, computed using the macroporosity, was $6.03 \times 10^{-8} \text{ m}^3$. We assume that the microporosity is water saturated throughout the experiment, as the oil pressure during wettability alteration—described in the next section—was not sufficiently high to invade the micropores. The sample was initialized with the injection of formation brine, prepared to mimic the chemical composition of the brine in a giant producing oil reservoir in the Middle East.

2.1. Establishing Wettability

A process called aging was performed to restore the wettability conditions typically encountered in hydrocarbon reservoirs (Alhammadi et al., 2017; Lin, Bijeljic, Krevor, et al., 2019). This was achieved using crude oil provided from the same producing reservoir from which the brine composition was taken. More information on crude oil composition are provided by Alhammadi et al. (2017). Pressure and temperature were raised to the conditions representative of an oil field deep underground (10 MPa and 80°C). Crude oil was then injected through the sample, increasing the flow rate stepwise from 0.01 to 0.1 ml/min at the bottom of the sample. The flow was then reversed, and more crude oil was injected at the top of the sample at the same flow rates. For a week, 5 PVs of crude oil were injected each day. The sample was then left at these conditions of high temperature and pressure for a month and then conserved in an oven in the crude oil at ambient pressure and 80°C for 2 months.

Table 1
Physical Properties of the Fluids Used in the Experiments

Phase	Density (kg/m ³)	Viscosity (mPa × s)	Interfacial tension (mN/m)
Water (H ₂ O + 20%w KI)	1,154.05	0.5471	$\sigma_{ow} = 52.1$
Oil (Decane + 15%w C ₁₀ H ₂₁ I)	715.2	1.088	$\sigma_{go} = 11.2$
Gas (N ₂)	83.98	0.01896	$\sigma_{gw} = 63.7$

Note. Densities measured at 40° and 7.6 MPa. Viscosities of nitrogen and water at 50° and 10 MPa are from Georgiadis et al. (2010) and of decane at ambient conditions are from the National Institute of Standards and Technology (2018). The interfacial tensions were measured directly using the pendant drop method (Alhosani et al., 2019; Li et al., 2012).

2.2. Experimental Fluids

After aging, the sample was transferred to the Diamond Light Source synchrotron facility in the United Kingdom, where the experiments were performed. The experimental fluids used were pure nitrogen, water doped with 20% by weight potassium iodide (KI) and decane doped with 15% by weight iododecane (C₁₀H₂₁I). These dopants provided sufficient difference in the X-ray attenuation of each phase, so that they could be distinguished in the final tomograms (Scanziani et al., 2018). The properties of the fluids used are listed in Table 1: The interfacial tensions were measured using the pendant drop method (Alhosani et al., 2019; Li et al., 2012).

2.3. Experimental Method

Figure 1 illustrates the experimental apparatus. The three-phase flow experiments were performed while imaging the sample using high-energy X-rays. The sample was mounted inside the core-holder (Figure 1) on top of a PEEK spacer, which was used during imaging to identify the exact times at which the fluids invaded the sample. Before starting the synchrotron tomography experiment, the oil was injected in the sample to displace and substitute the crude oil.

Pressure and temperature were then raised to the experimental conditions, 8 MPa and 50°C, and water injection (WF1) was started at 0.5 µl/min, corresponding to a capillary number $Ca = 3.3 \times 10^{-9}$ defined by $Ca = \mu q / \sigma$, where q is the Darcy flux per unit area, μ is the viscosity of the injected phase (doped brine, the

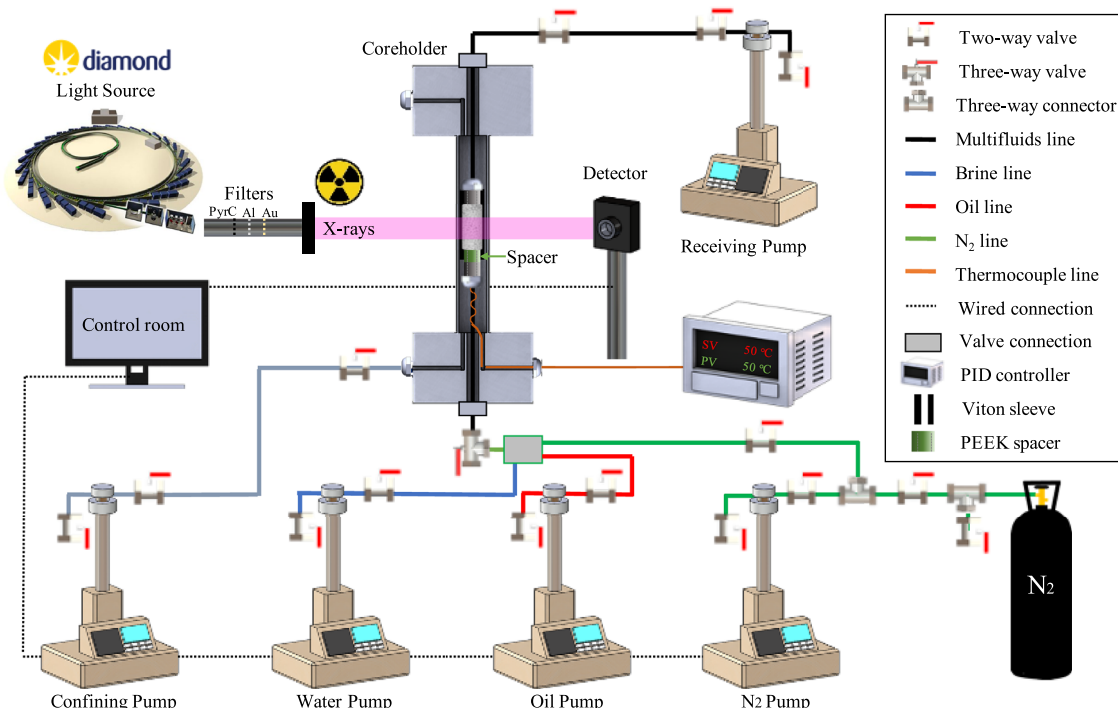


Figure 1. Schematic of the experimental apparatus comprising three injection pumps, a receiving pump, and a confining pump to maintain high fluid pressures. The sample is imaged using synchrotron X-rays.

Table 2
Experimental and Imaging Details

Displacement	Flow rate ($\mu\text{l}/\text{min}$)	Ca	PV	S_w	S_o	S_g
WF1	0.50	3.3×10^{-9}	0.6	0.34 ± 0.02	0.66 ± 0.03	-
GI	0.15	1.6×10^{-10}	0.2	0.33 ± 0.02	0.43 ± 0.03	0.24 ± 0.03
WF2	0.30	2.0×10^{-9}	0.3	0.38 ± 0.02	0.39 ± 0.03	0.23 ± 0.03

Note. The capillary number is defined by $Ca = \mu q / \sigma$, where q is the Darcy flux of the injected phase and μ is the viscosity of the injected phase. We used the oil-water interfacial tension σ_{ow} to calculate Ca during WF1 and WF2 and the gas-oil interfacial tension σ_{go} to calculate Ca during GI (see the values in Table 2). PV is the number of pore volumes injected. The saturations, S_w , S_o , and S_g are computed from the segmented images at the end of each injection.

water phase), and σ is the oil-water interfacial tension (see Table 2). All the injections were performed from the bottom of the sample. When water was detected in the PEEK spacer, dynamic imaging of the center of the sample (Figure 2) started. WF1 was stopped after 78 min (0.5 PV, injected), when no significant change in the pore space had been observed for at least 15 min. This was assessed by checking differential images between scans taken 15 min apart from each other: The flow was stopped when no difference was noticed between the two scans (the differential image showed noise only). Gas injection (GI) was then performed at a flow rate of $0.15 \mu\text{l}/\text{min}$ ($Ca = 1.6 \times 10^{-10}$ using the gas flow rate and viscosity and the gas-oil interfacial tension) for 92 min (0.2 PV). Second waterflooding (WF2) was then performed at $0.1 \mu\text{l}/\text{min}$ ($Ca = 2.0 \times 10^{-9}$ using the water flow rate and viscosity and the water-oil interfacial tension) for 204 min (0.3 PV).

2.4. Synchrotron Imaging

The imaging was performed at the DiamondManchesterImagingBranchline(I13-2). High-intensity X-rays were collected from the accelerator machine of the Diamond Light Source and brought to the beamline. Here, three filters (1.3 mm Pyrolytic C, 3.2 mm Al, and $10 \mu\text{m}$ Au) trimmed the wavelength of the X-rays to obtain a high-intensity pink beam (Marathe et al., 2019). The resulting X-ray spectrum has a thin peak at 15 keV, corresponding to a flux of 9×10^{12} photons per second (Rau et al., 2019). The distance between the sample and the camera was set to 12 mm, which provided optimal image quality.

High-quality static images were collected before and after each injection step, scanning the whole sample with three scans at the predetermined locations in the vertical direction, and these were later stitched together to obtain images of the whole sample (Figure 2). Each static image contains $1,280 \times 1,284 \times 1,080$ voxels. During the injections, dynamic imaging was performed at the middle of the sample in the vertical direction, as illustrated in Figure 2. The spatial resolution of all the images was $3.5 \mu\text{m}$, while each dynamic scan was taken every 74 s (WF1 and GI) or 80 s (WF2): The time required to acquire each scan is obtained

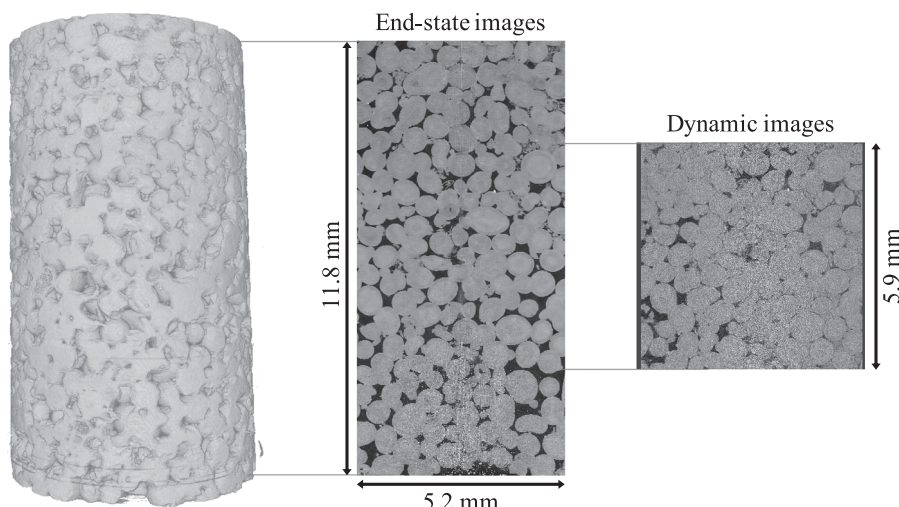


Figure 2. Static images were collected at the end of each injection, at three different locations in the vertical direction, and stitched together to obtain images of the whole sample. These images were used to compute saturation, Table 2. Dynamic images were acquired during the injections in a selected location at the center in the vertical direction.

Table 3*Details on the Time of Each of the Three Dynamic Imaging Steps*

Displacement	Time begin, time end (s)	Images	Projections (S–D)	Exposure time (S–D) (s)
WF1	0, 4,706	65	3,000–900	0.08–0.06
GI	5,627, 9,553	56	2,000–900	0.08–0.06
WF2	10,665, 18,074	106	3,000–1,000	0.08–0.06

Note. Three static scans were collected at the end of each step. The exposure time is the time taken to image one projection: A 3-D image is then constructed from all the projections. Values for number of projections and exposure time are reported for both S (static images) and D (dynamic images).

by multiplying the exposure time per the number of projections, provided in Table 3, with 20 s required to bring the sample back to the initial position and transfer the data from the detector to the workstation in the control room. Each of these dynamic images contains $1,280 \times 1,284 \times 1,080$ voxels.

We collected a total of 227 tomograms over the whole experiment. The time stamp of each injection sequence and the number of tomograms are listed in Table 4. The reconstructed images occupy a total of approximately 14 TB of memory.

2.5. Image Processing

The tomograms were reconstructed, obtaining 3-D gray scale images. Segmentation—the assignment of each voxel to a phase (rock, water, oil, or gas)—was then required to obtain the quantitative results presented in section 3.

The static scans were segmented using a seeded watershed segmentation algorithm (Jones et al., 2007). Prior to segmentation, these images were stitched together to obtain the full image of the sample and filtered with a nonlocal means filter (Buades et al., 2008; Schlüter et al., 2014). Injected water and gas were identified by subtracting the image obtained at the beginning of the experiment from images acquired at the end of WF1, GI, and WF2. The result was filtered again with the nonlocal means filter prior to performing watershed segmentation (Buades et al., 2008).

The dynamic images acquired during the injection of fluids were taken using a lower number of projections (see Table 3) to achieve higher time resolution. For this reason, another, more accurate but time consuming, segmentation method was required for these images: We used the machine learning WEKA segmentation method (Arganda-Carreras et al., 2017). The preliminary steps were similar, as we performed subtraction of the image at initial condition to each of the dynamic images. However, filtering was not required, as WEKA segmentation method has a filtering step embedded. A sample image was manually labeled to construct the training data set. A random forest machine learning method was then applied to the image that uses the training data set to classify all the voxels in the images. The details of WEKA segmentation are explained in Figure 3.

Table 4

In the First Three Rows: Mean Values and Standard Deviations of the Contact Angles Measured in Degrees at the End of Each Injection Step for Oil-Water (θ_{ow}), Gas-Oil (θ_{go}), and Gas-Water (θ_{gw}) Solid Contacts, Using the Method Developed by AlRatrou et al. (2017); in the Last Three Rows: the Number of Contact Points Where the Contact Angles Were Computed by the Method

Displacement	θ_{ow} (°)	θ_{go} (°)	θ_{gw} (°)	Predicted θ_{gw} , using Equation 2 (°)
WF1	109 ± 23.2	—	—	—
GI	105 ± 27.5	57.1 ± 25.7	80.7 ± 23.2	96.9
WF2	103 ± 27.4	57.1 ± 24.1	81.9 ± 22.3	95.3
	$N_{\theta_{ow}}$	$N_{\theta_{go}}$	$N_{\theta_{gw}}$	
WF1	180,944			
GI	319,882	167,174	47,193	
WF2	393,848	187,408	63,199	

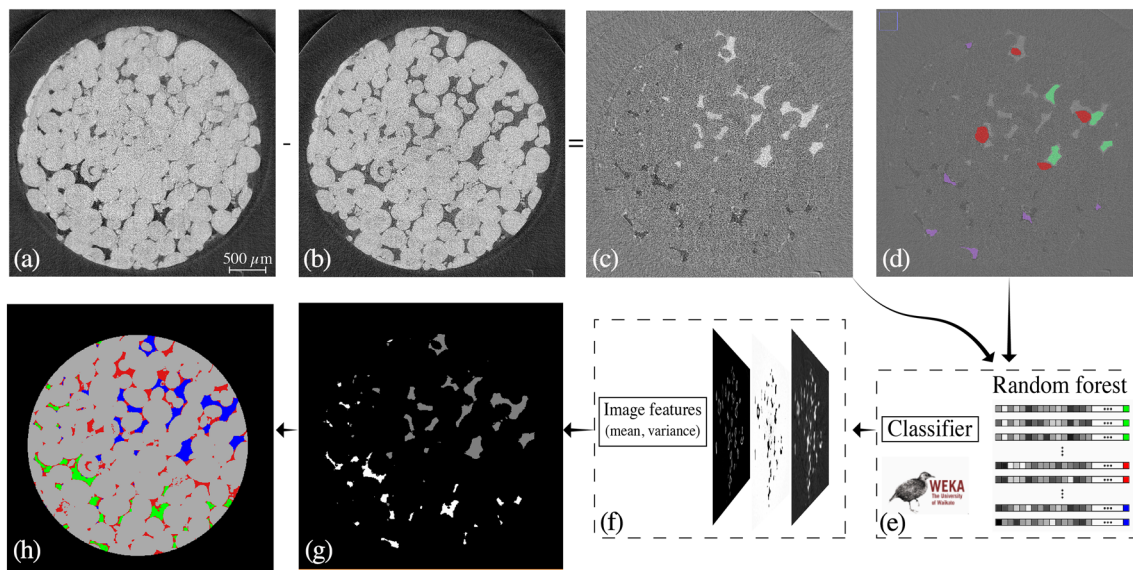


Figure 3. Workflow for image segmentation. (a) Image with four phases: gas, oil, water, and rock from darker to brighter. Rock and water have a similar attenuation coefficient. (b) Image taken before starting the dynamic experiment, with the sample filled with oil. Panel (c) is the differential image obtained subtracting panel (b) from panel (a): Gas-filled pores are black, while water-filled pores are white. Panel (d) represents the creation of the training data set, which is done on the differential image (c): Gas-filled pores were marked in purple, water-filled ones in green, and noninvaded regions in red. Panel (e) shows the WEKA machine-learning training algorithm, which takes panels (c) and (d) as input and creates a classifier. Panel (f) shows the image features on which the classifier is applied: These are the mean and variance of the gray scale values of the image. Panel (g) is the resulting segmented differential image, obtained using the classifier and the image features: Gas-invaded pores are white, brine-invaded pores are gray, and noninvaded pores are black. Panel (h) is the final segmented image, obtained by combining panel (g) with a segmented image of the sample before starting injection: Gas is green, oil is red, water is blue, and the rock is gray.

The two segmentation methods give comparable results when applied to the same images with low level of noise (Alhammadi et al., 2017; Garfi, John, Berg, et al., 2020). In contrast, for the dynamic images, the watershed segmentation did not provide accurate results, which were instead achieved using WEKA.

The segmented images were postprocessed to obtain quantitative results. The saturation of each phase was obtained from the images by computing the fraction of voxels assigned to the selected phase in relation to the total number of voxels assigned to the pore space. The water volume in microporosity was ignored in the analysis. Connectivity was obtained by selecting one phase and assigning its voxels to connected clusters (or ganglia).

To obtain information on the dimension of pore openings (pores) or restrictions (throats) occupied by each phase, the pore space was mapped using a generalized pore-network model (Raeini et al., 2018), obtaining sets of maximum balls representing pores and throats with their inscribed diameter. This *equivalent pore diameter* will be used as a proxy for pore dimension. Combining this map with the 3-D images of the pore space, pore and throat occupancies were obtained from identifying the phase that occupied the voxel at the center of the maximal ball (Scanziani et al., 2018). A similar maximum-ball concept was used to identify the local thickness of the oil phase and obtain the oil layer thickness: The maximum ball that can be inscribed in the space identified with oil in each location is the local oil thickness (Hildebrand & Ruegsegger, 1997).

The interface between the phases was identified as the surfaces meshed on voxels, which have neighbors assigned to different phases (interfacial voxels). The interface was smoothed to remove voxelization artifacts (Lin et al., 2018). The specific interfacial area was computed as the total area of the surface of the interface between two phases divided by the total volume of the rock (pore and grain).

We define the total curvature between phases i and j as κ_{ij} with a positive value when phase j bulges into phase i and use it to estimate the capillary pressure $P_{c,ij} = P_j - P_i = \sigma_{ij}\kappa_{ij}$ from the Young-Laplace equation (Laplace & Fournier, 1805), where σ_{ij} is the interfacial tension between phases i and j . There is a general constraint between the curvatures if the phases are connected:

$$\sigma_{ik}\kappa_{ik} = \sigma_{ij}\kappa_{ij} + \sigma_{jk}\kappa_{jk}. \quad (1)$$

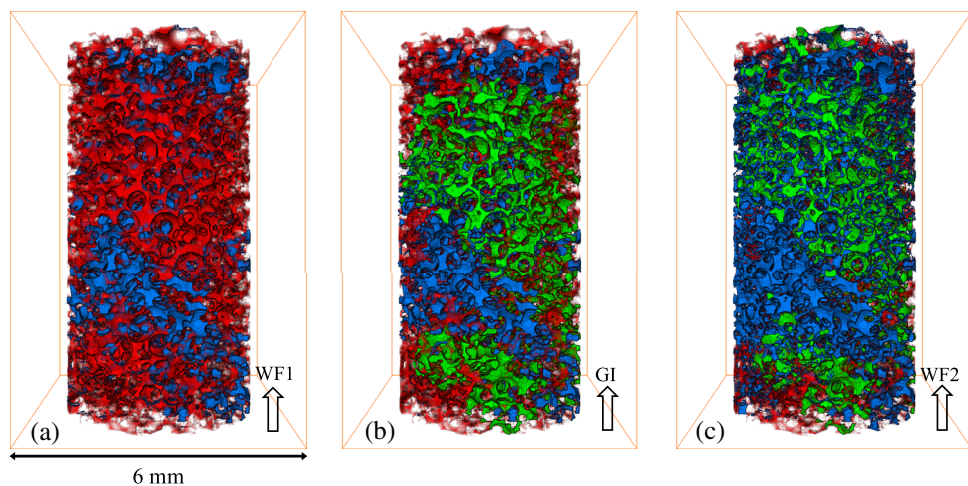


Figure 4. Three-dimensional rendering of oil (red), water (blue), and gas (green) at the end of (a) first waterflooding (WF1), (b) gas injection (GI), and (c) second waterflooding (WF2). The arrows show the direction of the injection of water and gas.

The total curvature is defined as the sum of the curvatures in the two principal directions, while the Gaussian curvature is the product of the two principal curvatures (Armstrong et al., 2012; Lin et al., 2018). When computing both Gaussian and total curvatures, we record the interfacial area-weighted average values.

3. Results and Discussion

We examine the pore-scale physics leading to either the enhancement of flow or trapping in mixed-wet porous media. The 227 tomograms obtained during the experiment were segmented as described in section 2.5 and used for computing pore-scale descriptors and to interpret the dynamics of three-phase flow and trapping in mixed-wet porous media. After a first waterflooding (WF1), gas was injected in the sample to study three-phase flow (GI), followed by further injection of water (WF2). The 3-D configuration of the phases at the end of each injection is illustrated in Figure 4.

First, in section 3.1, we characterize the wettability of the sample. In section 3.2, we study the dynamics of gas and water invasion during GI and WF2. Section 3.3 focuses on the formation and the thickness of oil layers, which allowed for oil recovery, and section 3.4 shows how gas is trapped in the pore space during WF2, ensuring a high remaining gas saturation (see Table 2). In section 3.5, we use the four Minkowski functionals of a 3-D object—volume, surface area, total curvature, and Gaussian curvature—to obtain a complete characterization of the dynamics of three-phase flow. The overall context of the work is how the wettability order controls the pore-scale fluid dynamics and the implication this has, in turn, for storage, recovery, and design applications.

3.1. Wettability Characterization

The wettability of the system has a strong influence on flow properties such as relative permeability and trapping (Alizadeh & Piri, 2014; Hui & Blunt, 2000; Piri & Blunt, 2005; Van Dijke & Sorbie, 2002). The direct measure of wettability, defined for two-phase flow, is the contact angle between the interface of the two phases and the solid (Andrew et al., 2014; AlRatnout et al., 2018; Rücker et al., 2019; Scanziani et al., 2017). The geometric oil-water contact angle for this sample was estimated using the method of AlRatnout et al. (2017) and resulted in a distribution of angles both lower and higher than 90° with a mean value of 109° at the end of WF1. This defines the system as mixed-wet, as both oil and water can in turn favorably wet the solid surface at different locations in the sample. Figure 5 shows the probability distributions of the geometric contact angles between the phases at the end of GI and WF2, while Table 4 reports their mean values. These values suggest that, on average, water is the nonwetting phase with respect to oil, oil is wetting to gas, while water and gas present an intermediate wettability between each other, with mean values of contact angle close to 90°. The skewness of the distributions is related to the mixed-wet nature of the sample: Contact angles tend to assume a wide range of values both lower and higher than 90°, but at the same time they cannot—by definition—be lower than 0° or higher than 180°. The automatic method used to estimate the

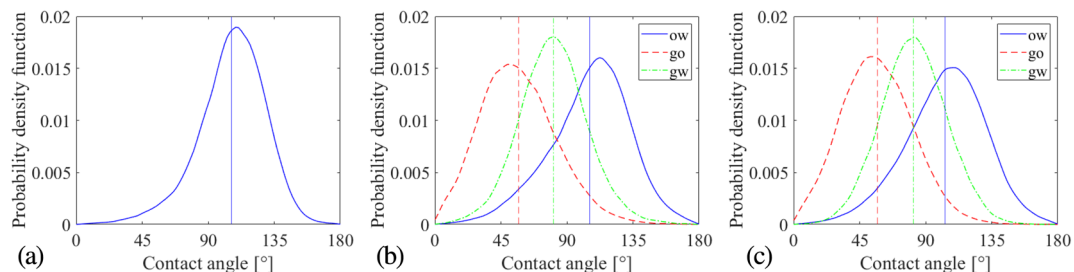


Figure 5. Estimations of probability density functions obtained from the histograms of the geometric contact angles, computed from the static images at the end of each injection: (a) WF1, (b) GI, and (c) WF2. The contacts angles are computed for oil-water (ow), gas-oil (go) and gas-water (gw) solid contacts. The vertical lines represent the mean values.

contact angles computes hundreds of thousands of angles for each image—as shown in Table 4—leading to the smooth distributions shown in Figure 5 (AlRatrou et al., 2017).

The contact angles in a three-phase system, θ , are not independent but must obey the Bartell-Osterhof constraint in equilibrium (Bartell & Osterhof, 1927; Van Dijke & Sorbie, 2003):

$$\sigma_{ik} \cos \theta_{ik} = \sigma_{ij} \cos \theta_{ij} + \sigma_{jk} \cos \theta_{jk}, \quad (2)$$

for any phases i, j , and k .

We use the interfacial tension values in Table 2 and the mean contact angles presented in Table 4 to predict the gas-water contact angle from the measured oil-water and gas-oil values (Van Dijke & Sorbie, 2002). There is a difference of about 15° between the observed and predicted values: The direct measurements imply that on average, gas is nonwetting to water (albeit weakly so), while the predictions of Equation 2 suggest that gas is slightly wetting to water. However, the Bartell-Osterhof Equation 2 is defined for three phases in equilibrium at the same location in a system with constant wettability. This is not the case for the mixed-wet medium studied here, where it has been shown that contact angles are variable in space and wettability is not constant through the whole sample.

Furthermore, the contact angles are measured at static conditions and so may represent hinging angles on rough or altered-wettability surfaces, rather than contact angles for a displacement process (Blunt et al., 2019). In particular, it is possible that high hinging oil-water contact angles are measured at the end of WF1, when the water pressure is high. These values, which do not represent the angles during a displacement, particularly at the early stages (Scanziani, Lin, et al., 2020), persist in later injection sequences, which leads to an overprediction of the actual gas-water contact angles using Equation 2. However, this still represents some ambiguity in the wettability order: Is gas more or less wetting than water?

In three-phase flow, the wettability order establishes which of the three phases more favorably flows on the surface of the rock grains and in which order the other phases tend to reside in the center of the pores and where they can be trapped. Using the directly measured values of contact angles described previously, we notice that oil is wetting to both water and gas, water is nonwetting to oil and neutrally wetting to gas, while gas is nonwetting to oil and neutrally wetting to water. We would then expect that oil is the most wetting phase and gas and water are both, on average, nonwetting.

To further clarify the wettability order of the system, we used pore occupancy (Figure 6), fluid-solid interfacial areas (Figure 7a), and visual inspection (Figures 7b and 7c).

Pore occupancy has been previously used in three-phase flow to describe the arrangement of the three phases in the pore space (Alhosani et al., 2019; Scanziani et al., 2018). Figure 6 shows the pore occupancy at the end of each injection. We observe that we do not have a clear definition of most and least wetting phases. Water occupied pores of a wide range of sizes, while oil and gas preferentially resided in smaller and wider pores, respectively. Using the mean value of the diameter of the pores occupied by each phase at the end of WF2, when all the phases have a similar saturation (Table 2), we can establish an approximate wettability order: oil-, water-, and gas-occupied pores had an average diameter of 35.7 ± 24.9 , 49.4 ± 33.6 , and $79.1 \pm 24.5 \mu\text{m}$, respectively. Using these values, we can suppose an oil-water-gas wettability order, from most to least wetting, but the high standard deviations suggest that there is a mix of wettabilities, as evident in WF1, with regions of the pore space that are wetting to oil and regions that are water-wet.

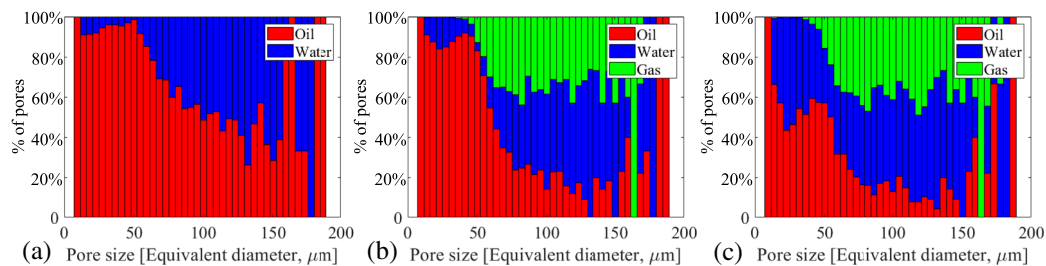


Figure 6. Pore occupancy at the end of (a) WF1, (b) GI, and (c) WF2.

The pore occupancy quantification method described above searches for the phase residing in the center of the pores. With a different approach, we can study which phase preferentially wets the surface of the grains (Garfi, John, Lin, et al., 2020). Figure 7a shows the interfacial area, specific to volume, between each of the three phases and the solid surface, computed from the segmented images, throughout the injection sequence. Oil was the phase with highest interfacial area with the solid at all times, confirming that it is, on average, the most wetting phase. This area decreased as gas was injected in the sample, but was still twice the area between water or gas and the solid, even when the oil saturation approached the water saturation at the end of GI (Table 2). The gas-solid interfacial area increased as gas was injected, approaching the water-solid value. Since the gas saturation at the end of GI was still lower than the water saturation (0.23 vs. 0.37), we cannot definitely state that gas was less wetting than water, as its lower interfacial area with the solid would suggest. However, this approach again suggests an average oil-water-gas as the wettability order, consistent with the measured contact angles and assessment of pore occupancy.

Another indication of the wettability order can be inferred from direct visual inspection of the images of the rock and the fluids (Figures 7b and 7c). In the circled example of Figure 7b, as we noticed in many other locations in the pore space, an approximately flat interface between gas and water is shown, with a contact angle close to 90°. This suggests neutral wettability between these two fluids, which is consistent with the gas-water contact angle, the occupancy of pores of similar size (Figure 6), and similar fluid-solid interfacial area (Figure 7a), described earlier. In the squared detail of Figure 7b, we observe the presence of oil layers, wetting the solid surface. This is again consistent with the occupancy of pores of similar size and large oil-surface interfacial area, supporting the argument of oil being the most wetting phase. The formation and thickness of layers will be discussed in section 3.3. **In Figure 7c, gas-oil and water-oil interfaces are shown, where oil is wetting to both water and gas.**

All the different methods of wettability characterization illustrated above (contact angles, pore occupancy, fluid-solid interfacial area, and visual inspection) consistently suggest an average oil-water-gas wettability order. However, the geometrical and chemical complexity of the pore space of rocks with altered wettability allows for a spatial variability of wettability through the sample, resulting in wide distributions and high

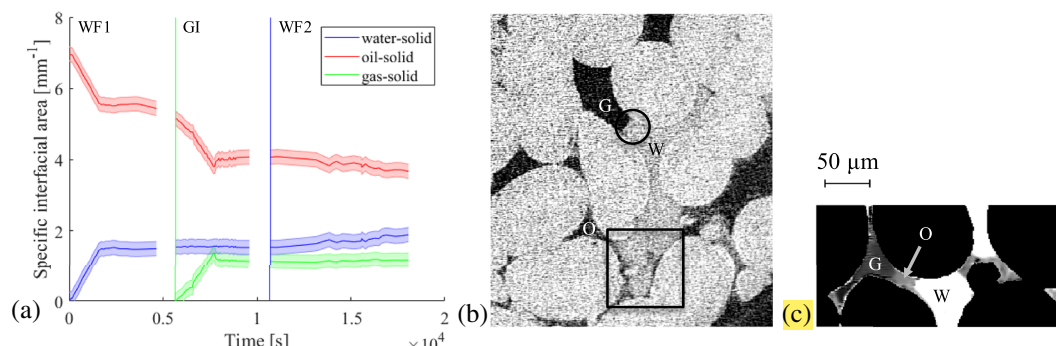


Figure 7. (a) The interfacial area between each phase and the solid, normalized to the total image volume; the width of the lines indicate the uncertainty in the measurements, estimated by using different training data sets for segmentation. (b) Two-dimensional slice of the gray scale image at the end of WF2, where G is gas, W is water, and O is oil. (c) Another slice of the gray scale image at the end of WF2, where the rock phase has been masked out for easier visual inspection. G is gas, W is water, and O is oil.

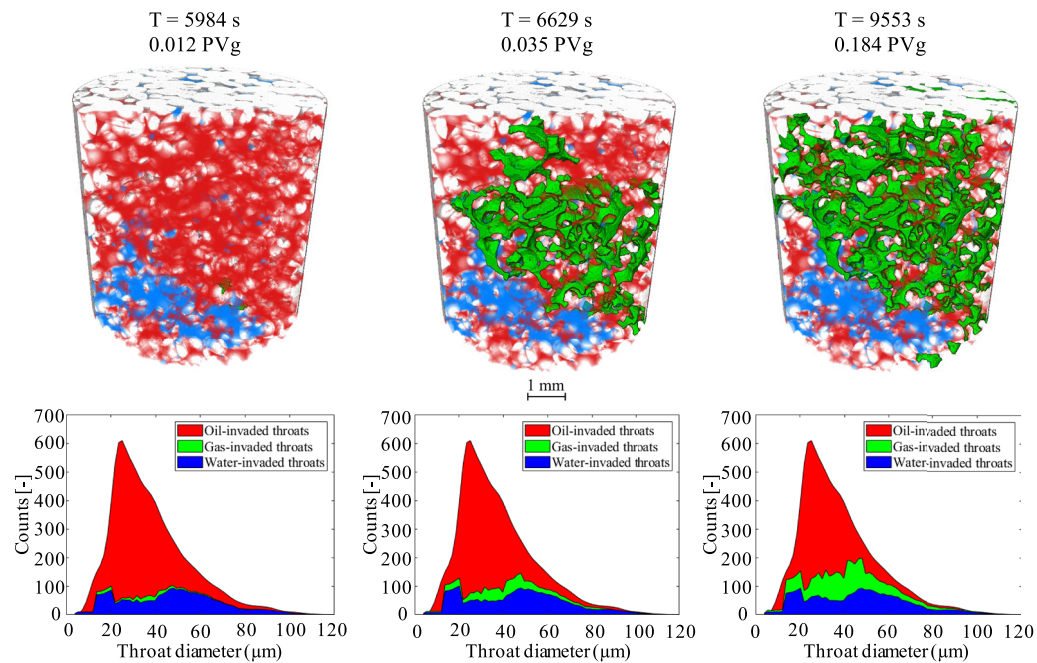


Figure 8. Top row: 3-D rendering of the rock (light gray), oil (red), water (blue), and gas (green) at different times during GI. Bottom row: area chart showing the distribution of throat size and their occupancy. PVg indicates the pore volumes of gas injected at each time step.

standard deviations for contact angles, pore occupancy, and interfacial areas. This variability defines the system as mixed-wet and allows for complex behavior of multiphase flow, with regions of the pore space that are, locally, more water-wet and, at the other extreme, regions where water is nonwetting to gas.

3.2. Dynamics of Three-Phase Flow

Having defined the system as mixed-wet, with an average wettability order oil-water-gas, in the next sections, we will describe the dynamics of three-phase flow during the injection steps and how some key pore-scale descriptors—related to the [Minkowski functionals](#)—dynamically changed during the injections. A complete description of the dynamics of WF1 is provided by Scanziani, Lin, et al. (2020), while here we will focus on gas injection and second waterflooding, where three-phase flow is present.

3.2.1. Gas Injection

The principal displacement process during gas injection was direct piston-like displacement of oil by gas (top row of Figure 8). This contrasts with the observations made in a weakly oil-wet sample (Qin et al., 2019) and in a previous study using the same Ketton rock under water-wet conditions (Scanziani, Lin, et al., 2020) where double displacement events—when one phase displaces a second which displaces a third—were common, in particular double drainage where gas displaced oil that displaced water (Øren et al., 1992). The reason for this is the wettability of the system. After contact with crude oil, much of the pore space becomes oil-wetting (see Figure 5). This means that at the end of waterflooding, the capillary pressure $P_{cow} = P_o - P_w$ is negative—the water pressure is *higher* than the oil pressure, as water has to be forced into the pore space. When gas is now injected, gas will fill pores for whom the entry pressure allows invasion at the lowest gas pressure. If P_{cow} remains unchanged, then it is more favorable for gas to displace oil, as it has a lower pressure than water, especially as gas is nonwetting to water in most of the pore space and has to have a higher pressure than water to displace it. Double displacement is suppressed thanks to contact angle hysteresis: The contact angle for oil to reinvoke water occupied pores is likely to be lower—meaning less favorable displacement—than during waterflooding (Morrow, 1990). This interpretation of the results will be confirmed later when we quantify capillary pressures.

The bottom row of Figure 8 shows the occupancy of the throats or restrictions in the pore space during GI: This contrasts with Figure 5, which showed the occupancy of the wider regions, pores. At the end of WF1, water had invaded a wide range of throat size (Scanziani, Lin, et al., 2020), as a signature of mixed wettability. The injected gas, being the most nonwetting phase, would be expected to invade the largest

throats preferentially. However, even if most of the largest throats were indeed invaded by gas at the end of GI, gas also invaded some smaller throats; this is most noticeable at the beginning of GI. The reason for this behavior is twofold: First, not all the throats are available for displacement at any time, as some throats are either far from the gas front or occupied by water (hence requiring higher capillary pressure). Second, the wettability of the sample is not constant in space, but this is instead characterized by a wide spatial distribution of contact angles (Figure 5). This means that some smaller throats which are less nonwetting to gas will fill preferentially to larger throats where the gas-oil contact angle is closer to zero.

3.2.2. Second Waterflooding

Again, unlike the water-wet case, the principal displacement process during WF2 is direct displacement of oil by water; there is little contact between water and gas, as the gas is surrounded by wetting and spreading layers of oil—described in the next section. We observed some double displacement events—water-gas-oil—as seen in water-wet rocks as well (Scanziani et al., 2018; Scanziani, Singh, et al., 2020), where water displaces oil that traps gas. This causes oil layers to swell and trap gas by snap-off. A detailed description of this trapping mechanism will be provided in section 3.4.

3.3. Layers

In this section, we will study oil layers since they can enhance oil connectivity and flow while facilitating the trapping of water and gas. From Table 1, we can define a spreading coefficient C_{si} for phase i in the presence of phases j and k as follows (Blunt, 2017; Hirasaki, 1993):

$$C_{si} = \sigma_{jk} - \sigma_{ij} - \sigma_{ik}. \quad (3)$$

Using the values in Table 2, we calculate an oil spreading coefficient $C_{so} = 0.2 \text{ mN/m}$. This is close to zero and indicates that it is possible for oil to spread between water and gas in the pore space. Furthermore, under oil-wet conditions, the oil can reside next to the solid surface with gas or water occupying the center of the pore space.

At near-miscible conditions, when the properties of the gas and oil are similar, it is possible to observe layers of gas (Alhosani et al., 2020). However, in our experiments, where oil and gas are immiscible, using Equation 3 and Table 2, $C_{sg} = -22.7 \text{ mN/m}$, which is large and negative, indicating that gas layers will not form. The spreading coefficient for water, the intermediate wetting phase, is even larger and more negative ($C_{sg} = -104.7 \text{ mN/m}$), making it very unfavorable for water layers to exist.

The arrangement of a phase in layers causes an increase in its connectivity, allowing the flow in the pore space at low relative permeabilities. For three-phase flow in a water-wet medium, with a wettability order water-oil-gas from most wetting to most nonwetting, spreading oil layers have been observed (Scanziani et al., 2018). However, with the same wettability order, under near-miscible conditions, oil layers were not observed during gas injection, with oil and water confined to the smaller pores (Alhosani et al., 2019).

In this system, we did not observe any layers of gas, as the gas was not everywhere the intermediate wetting phase and had a large and negative spreading coefficient. Gas competed with water to occupy the center of the medium and larger pores. Instead, we observed oil layers. However, these usually did not spread sandwiched between water and gas, as it happens in water-wet systems (Scanziani et al., 2018), but mostly adhered to the surface as thick wetting layers next to the solid surface (as in the square of Figure 7b).

Figure 9 shows a 3-D representation of connected oil in a subset of the image (top row), at the end of WF1, GI, and WF2. We define a wetting layer a portion of oil with thickness lower than $30 \mu\text{m}$, as thicker volumes more likely correspond to bulky chunks of oil filling pores of small or medium size. We could only visualize layers thicker than the image resolution ($3.5 \mu\text{m}$).

Visible oil layers were present at the end of each injection step. However, we observe fewer and thinner layers at the end of WF1, since the water pressure was high, forcing oil into smaller regions of the pore space and squeezing layers closer to the solid surface. The injection of gas allowed the formation of more layers, increasing oil connectivity (e.g., in the circle of Figure 9b).

The second row of Figure 9 shows how the thickness of these layers changed during the three injection steps. At the end of WF1, the mean thickness of connected oil layers—locally measured as the diameter of the maximum ball which can be inscribed in the 3-D space segmented as oil—was $13.3 \pm 9.1 \mu\text{m}$. During GI, the thickness of the layers which were already present increased, as shown by the colors in Figure 9e,

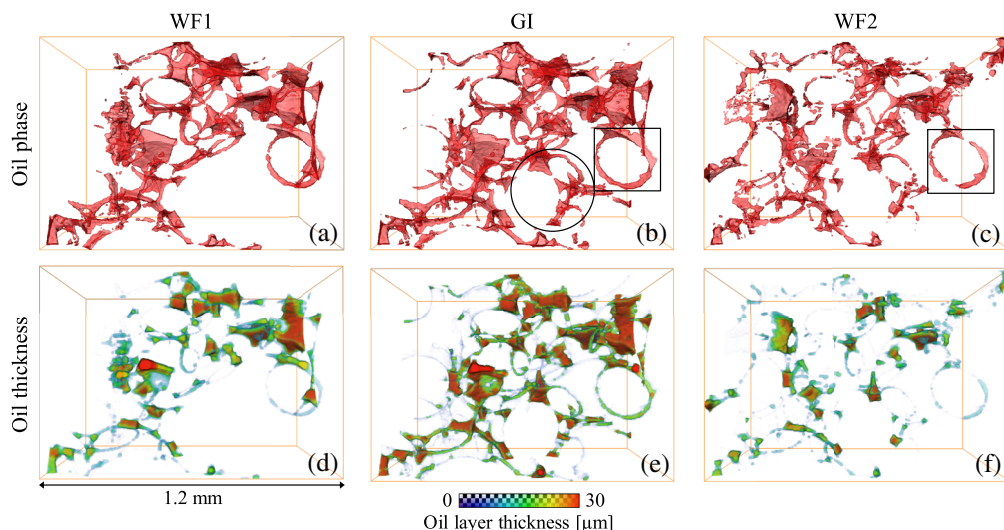


Figure 9. (a–c) Three-dimensional rendering of the connected oil phase in a subset of the rock at the end of WF1, GI, and WF2, respectively. In the circled region of panel (b), we highlighted the formation of new oil layers during GI. (d–f) Thickness map of the oil phase represented in panels (a)–(c).

while the formation of new thinner layers meant that the average thickness did not change significantly ($13.0 \pm 9.2 \mu\text{m}$). During WF2, more oil was drained from these connected layers, as again water-displaced oil, which decreased the layer thickness to a mean value of $10.2 \pm 6.7 \mu\text{m}$.

3.4. Gas Trapping

After gas injection, the gas was not produced and its saturation remained approximately constant when water was reinjected during WF2 (see Table 2). As it is mentioned in the previous section, during WF2“ water mainly contacted and displaced oil, with much less direct interaction between water and gas. However, gas is indirectly affected by water injection through water-oil-gas double displacements. These double displacements have an interesting consequence: Oil wetting layers swell in small regions of the pore space—throats—and trap the gas by snap-off, disconnecting the gas phase in immobile ganglia that prevent gas production.

A similar gas trapping during WF2 was observed in water-wet experiments in similar rocks (Scanziani et al., 2018; Scanziani, Singh, et al., 2020). However, there are some fundamental differences between the two cases. In water-wet media, the wettability order is water-oil-gas, and at immiscible conditions, oil spreads in layers, sandwiched between wetting water and nonwetting gas. The gas trapping events in these water-wet systems are double capillary trapping events, with water trapping oil which traps gas. The three-phases in fact coexist in the same pores, with the trapped ganglia of gas surrounded by spreading oil layers which are in turn surrounded by water wetting layers.

In the mixed-wet system presented in this work, instead, the wettability order is oil-water-gas (section 3.1), and the intermediate wetting phase, water, does not spread in layers, as its spreading coefficient is very negative (section 3.3). The gas snap-off events, hence, were the consequence of single capillary trapping of the most nonwetting phase (gas) by the most wetting phase (oil), similar to what happens in two-phase flow (Singh et al., 2017; Wildenschild et al., 2011).

An example of these events is shown in Figure 10. We monitored a subset of the image during WF2. A fingerprint of water injection can be observed in the squared throat: Water was trying to invade the small throat as its pressure increased while water was injected in the sample.

The circled throat, instead, presents an example of the double displacements mentioned above: First, at $T = 15,789 \text{ s}$, gas was pushed in the throat and in the adjacent pores through a double displacement (water-oil-gas), and later ($T = 15,931 \text{ s}$) oil snapped off the gas occupying the circled throat and confining it as a disconnected cluster, trapped in the pore space.

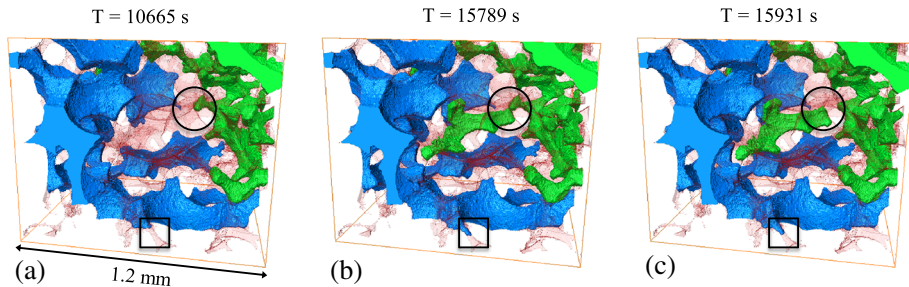


Figure 10. Three-dimensional representation of the fluids occupying the pores of a subvolume from the dynamic images, at three time steps (a), (b) and (c) during WF2. Water is blue, gas is green, and oil is in semitransparent red. In the circled throat, gas invasion is highlighted (b) with subsequent gas trapping by oil (c), while the square shows a signature of WF2: water invading a small throat as its pressure increased during injection.

This trapping mechanism within pores has consequences at larger scales: The total amount of gas trapped in this immiscible mixed-wet system was very high, with almost no production of the injected gas (Figure 11a). Previous studies have shown that, in water-wet media, gas trapping by water is higher in the presence of oil than in simple gas-water systems, as the presence of oil inhibits the direct gas-water contacts, favoring capillary trapping over piston-like displacement of gas by water. This allowed the amount of gas trapped, in three-phase systems, to increase to 60% of the gas injected, with respect to values around 50% for two-phase systems (Scanziani, Singh, et al., 2020).

The increase of gas trapping to almost 100% of the gas injected observed in this study has to be attributed to the strikingly distinct dynamics of three-phase flow in mixed-wet media: As observed in section 3.2, during WF2, water preferentially displaced oil, rather than directly contacting gas, as gas was surrounded by wetting and spreading layers of oil. While water displaced oil, these layers swelled in small throats like the one circled

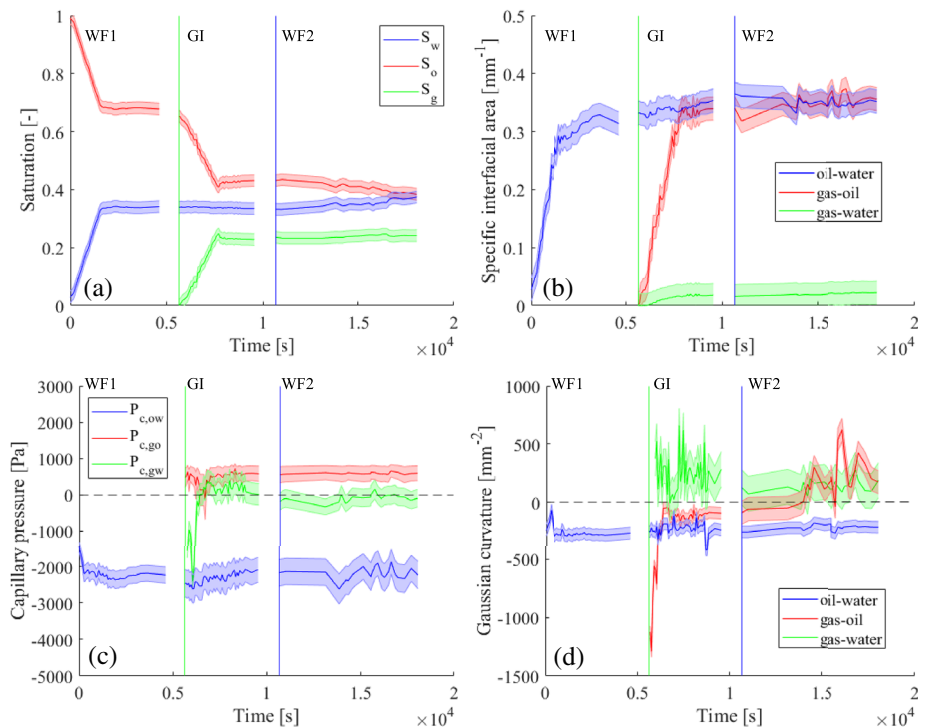


Figure 11. (a) Dynamic changes in saturations, (b) interfacial areas specific to the total volume, (c) capillary pressures, and (d) Gaussian curvatures between the phases involved in the experiment. The shadowed regions indicate the measurement uncertainty, obtained by using different training data sets for segmentation, and vertical lines show when each injection started. Horizontal dashed lines were added to the capillary pressure and Gaussian curvature plots to help distinguish between positive and negative values.

in Figure 10, trapping the gas. The gas in the pore space was then trapped as just described or bypassed, since water preferentially displaced oil, as we quantify later by computing gas-water interfacial area. As a result, gas storage is favored in immiscible mixed-wet three-phase systems, with respect to water-wet three-phase systems, which in turn presented enhanced gas trapping with respect to the two-phase case. This conclusion can have a considerable impact for gas storage applications, as discussed later.

3.5. Pore-Scale Descriptors (Minkowski Functionals)

For a detailed elucidation of the dynamics of gas injection, we computed saturation, interfacial area, capillary pressure, and Gaussian curvatures, which can be related to the Minkowski functionals, providing a complete description of the geometry of the phases in the pore space (Armstrong et al., 2018; Lehmann et al., 2008; Mecke & Stoyan, 2000; Scanziani, Singh, et al., 2020).

3.5.1. Saturations

During WF1, water invaded a wide range of pore sizes, displacing and producing oil with a displacement pattern controlled by wettability (Scanziani, Lin, et al., 2020). After the injection of about 0.5 PV of water, the injection was stopped and the water and oil saturation were respectively 34.2% and 65.8% (Figure 11a and Table 2). Subsequent injection of gas lowered the oil saturation to 43.2%, the gas saturation increased to 23.8%, while the water saturation did not change substantially, as gas mainly contacted oil (section 3.2). Second waterflooding (WF2) caused a further decrease of oil saturation to 38.5% and an increase in water saturation to 38.6%, without a considerable change in gas saturation, due to a significant amount of gas trapping (section 3.4).

These results suggest that immiscible gas injection, alternated with water injection, is an effective method to increase oil recovery: The total recovery factor, with respect to initial oil saturation, is 60.7%. In addition, the injected gas is retained in the pore space of the rock and was not displaced by a further injection of water: Almost all the gas is not produced, as it is trapped by oil in the pore space (section 3.4). This is promising for gas storage applications, as it suggests that chase water injection can rapidly and effectively trap the gas, ensuring secure sequestration.

3.5.2. Interfacial Areas

While saturation is related to the zeroth-order Minkowski functional (the volume), the interfacial area is the first-order functional (Armstrong et al., 2019; Lehmann et al., 2008). The interfacial area between the phases, which was computed from the segmented images and divided by the total volume to obtain the specific interfacial area, and its evolution during the experiment are shown in Figure 11b.

The interfacial area between oil and water increased as water was injected during WF1 and hence contacted the oil already present in the pore space. During GI, the interfacial areas again show that the injected gas mainly contacted oil (section 3.2), causing a steep increase in the gas-oil area, while the oil-water area only slightly increased due to double gas-oil-water displacements. Throughout the displacement, the gas-water area remained very low, indicating limited direct contact between gas and water: Their contact was prevented by the presence of wetting and spreading oil layers (section 3.3). During WF2, the interfacial areas did not change substantially, with the exception of an increase in the gas-oil area due to the multiple gas trapping events described in section 3.4.

3.5.3. Capillary Pressure

The second-order Minkowski functional is the total curvature of the interfaces between two phases, κ_{ij} . This was computed from the segmented images following the methods developed in previous work (Armstrong et al., 2012; Lin et al., 2018) and can be used to obtain the capillary pressure using the Young-Laplace equation $P_{c,ij} = \sigma_{ij}\kappa_{ij}$ (section 2.5). Using the values of σ_{ij} reported in Table 1, we obtained the capillary pressure between the three phases during the three injection steps (Figure 11c).

The negative capillary pressure between water and oil is a consequence of the oil-wet tendency of the sample, as indicated by oil-water mean geometric contact angles higher than 90° (Figure 5 and Table 4). A negative $P_{c,ow}$ indicates that $P_w > P_o$ as water has to be forced into the oil-wet pores. The oil-water capillary pressure remains negative throughout the displacement. It does increase (become less negative) during gas injection, consistent with the slight swelling of oil layers (see Figure 9). During WF2, the capillary pressure stays approximately constant, albeit with fluctuations, even though water continues to displace oil.

The gas-oil capillary pressure remains approximately constant once gas is injected, indicating that gas needs to reach a threshold pressure to displace oil and, during WF2, to be trapped. The capillary pressure is positive, since gas is nonwetting to oil.

The gas-water capillary pressure is the most interesting, since it assumes both positive and negative values. This strengthens the observation that gas and water compete to be the most nonwetting phase. Initially, during GI, the capillary pressure is negative, as gas will preferentially invade regions of the pore space where it is wetting to water (this is an imbibition displacement). However, as evident from the saturation, the amount of direct displacement of water by gas is limited. Later, the gas-water capillary pressure becomes positive, indicating that gas reaches regions of the pore space where it is nonwetting to water. During WF2, the capillary pressure is approximately zero to within the uncertainty of the measurements, indicating no clear wettability preference. Again, however, the amount of direct displacement of gas is limited, as the gas is trapped by oil.

Unlike conventional capillary pressure measurements, our curvature-based analysis includes all interfaces, capturing both connected phases and trapped clusters. As a result, Equation 1, which states that the gas-water capillary pressure is the sum of the oil-water and gas-oil values, is only obeyed when all three phases are connected. This is only seen at the beginning of GI: Later, water is trapped by gas, and then, during WF2, gas is trapped by water. This change in connectivity can be quantified through the Gaussian curvature, discussed next.

3.5.4. Connectivity and Gaussian Curvature

To study the potential mobility of each phase we computed their connectivity. In Figure 12, a different color is assigned to disconnected clusters of each phase. This representation shows that oil was connected during the whole experiment. This is in contrast with previous studies of water-wet systems, where WF1 and WF2 caused the segregation of oil in many disconnected ganglia (Singh et al., 2016, 2017; Scanziani, Singh, et al., 2020). The oil stays connected next to the pore walls as the most wetting phase, spreading in wetting layers of variable thickness (section 3.3).

The connectivity of water was also high as it was the injected phase during WF1 and WF2. Some water is trapped in pores of intermediate size during GI, but, as gas mainly displaced oil, there was not much change in the configuration of water (section 3.2). Gas connectivity decreased during WF2, as the injection of water caused the fragmentation of gas into disconnected ganglia. This did not allow high gas recovery and prevented its production with further water injection (section 3.4).

The third-order Minkowski functional, the Gaussian curvature of the interfaces, as a result of the Gauss-Bonnet theorem is directly linked to the Euler characteristic of a 3-D object, which quantifies its connectivity (Vogel et al., 2010). As a consequence, negative values of Gaussian curvature indicate a well-connected object, while positive values indicate ball-shaped objects or trapped clusters (Armstrong et al., 2019; Blunt, 2017).

The Gaussian curvature between the phases during the experiment is shown in Figure 11d. As evident in Figure 12, both water and oil remain connected throughout the displacement, and hence we see a negative Gaussian curvature between these two phases in Figure 11d. Hence, even though the sum of the curvatures, represented by the capillary pressure in Figure 10c, is negative, on average one curvature is positive while the other is larger and negative. This is a topological constraint to allow the phases to remain continuous. The Gaussian curvature between gas and water appears more noisy: As previously discussed, a small number of interfaces were formed between these two phases during the experiment (Figure 11b). At the beginning of GI, it is negative, since both gas and water are well connected. It increases and assumes a mainly positive value later as first some water is trapped, and then gas is trapped during WF2.

The gas-oil Gaussian curvature is most interesting and mirrors the connectivity of the gas phase. During GI, it is negative (Figures 11d and 13e), indicating that both the oil and gas phases are connected (see Figure 12). During WF2, it becomes positive, as gas is trapped and assumes, on average, a more spheroid shape.

Figure 13 shows the gas-oil curvature and quantifies how the curvatures in the principal directions κ_1 and κ_2 (where we define $\kappa_1 \geq \kappa_2$) evolved during GI and WF2. From these two curvatures, the total curvature $\kappa = \kappa_1 + \kappa_2$ and the Gaussian curvature $\kappa_g = \kappa_1 \times \kappa_2$ are calculated. At the beginning of GI (Figures 13a and 13e; when $T = 5,770\text{ s}$), κ_1 and κ_2 have opposite signs, leading to negative Gaussian curvature, meaning high connectivity of gas while it is injected; this connectivity was maintained until the end of gas injection

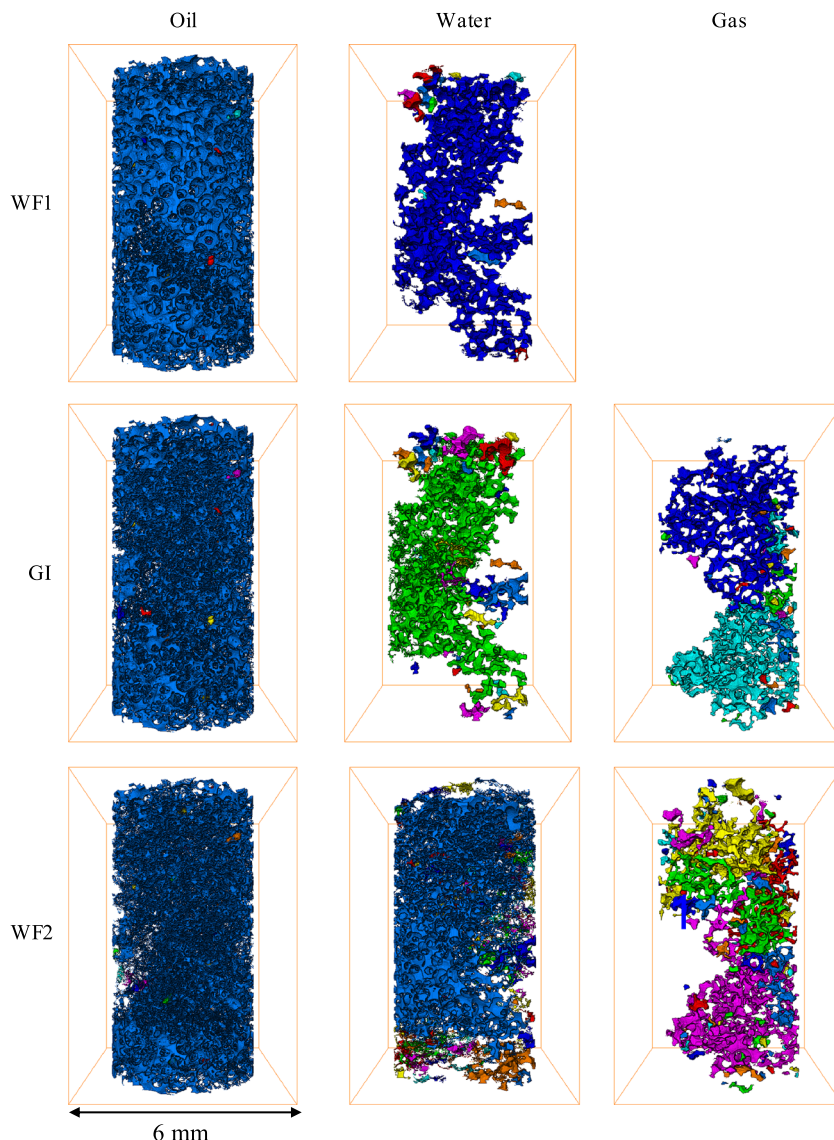


Figure 12. Connectivity of oil, water, and gas at the end of the first waterflooding (WF1), gas injection (GI), and second waterflooding (WF2). Different colors represent disconnected clusters of the same phase.

(Figures 13b and 13f; $T = 9,553$ s). Later, during WF2 (Figures 13c and 13g; $T = 13,872$ s), gas become less connected and κ_2 approached zero values, indicating a flat interface in one direction, which leads to a zero Gaussian curvature. Then later, all the curvatures became on average positive at the end of WF2 with a positive Gaussian curvature as the gas was trapped (Figures 13d and 13h; $T = 18,074$ s).

Notice that this significant shift in the product of the curvatures occurs while the sum of the curvatures, see the dashed distributions of Figures 11a–11d, was on average approximately constant, as the gas-oil capillary pressure did not change significantly (Figure 11c).

The change in κ_1 and κ_2 physically represents an evolution of the shape of the oil-gas interface. An example of a shape with curvatures with opposite signs in the two directions during GI can be observed in the squared region of Figure 9b, where the oil formed a loop while wetting a solid grain. The interface with gas at this location had a negative curvature in one direction, following the shape of the loop, and a positive value in the other direction, as gas bulges into oil. When later water was injected, the multiple displacements described in section 3.4 caused the rupture of the gas-oil interface, Figure 9c, changing the shape of the curvature which became on average positive in both directions (Figure 13d), resulting in gas trapping.

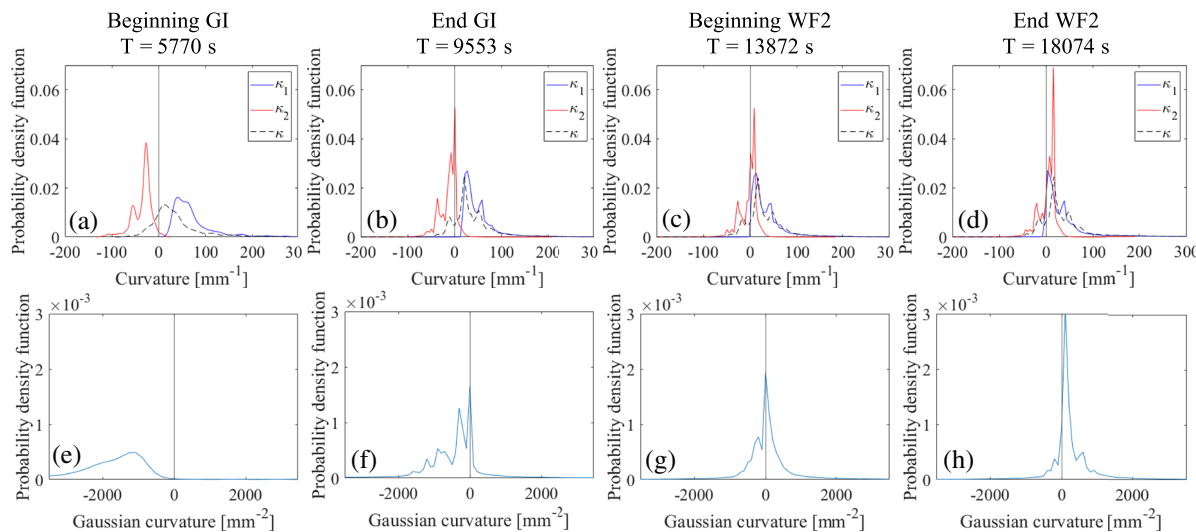


Figure 13. Focus on the gas-oil curvatures at four different times of the experiments (refer to Table 3). (a–d) Probability distributions of the curvatures κ_1 and κ_2 at the gas-oil interface in the two principal directions, along with the total curvature $\kappa = \kappa_1 + \kappa_2$. (e–h) Gaussian curvatures $\kappa_g = \kappa_1 \times \kappa_2$. The probability density functions are based on point measurements on the whole images. The resulting histogram is normalized such that the area under the curves sums to 1.

Overall, the capillary pressures and Gaussian curvatures provide a quantification of the key new features of three-phase flow uncovered in these experiments. In this mixed-wet system, while there are regions of the pore space that are water-wet, overall oil behaves as the most wetting phase with a negative oil-water capillary pressure and good connectivity, demonstrated by the negative Gaussian curvature of the oil-water interfaces. Gas is nonwetting to oil, and hence the gas-oil capillary pressure is positive: The Gaussian curvature of the gas-oil interface reflects the connectivity of the gas phase, being negative during GI and assuming positive values during WF2 when gas is trapped. Gas and water compete to be the most nonwetting phase with no clear wettability order: There are few direct gas-water contacts, the gas-water capillary pressure can be both less than and greater than zero, while the Gaussian curvature is positive when either water or gas are trapped.

4. Conclusions with Implications for Storage and Recovery

We have studied the dynamics of immiscible gas injection followed by waterflooding in a mixed-wet carbonate rock sample using synchrotron X-ray imaging with high spatial and temporal resolution. We have characterized the wettability of the system measuring contact angles, pore occupancy, and fluid-solid interfacial areas. As a result, the rock presented a mixed-wet behavior with oil-water-gas wettability order, from the most to the least wetting phase. However, there is a range of wettability across the rock, with regions that are water-wet. Furthermore, the gas is not clearly nonwetting to water, and again some of the displacement occurs when gas appears to be the intermediate-wet phase.

We have shown that the displacement process is strikingly distinct from that observed in a similar water-wet system. In particular, gas directly displaced oil with negligible displacement of water, unlike in a water-wet medium, where double drainage, where gas displaces oil that displaces water, is common. During subsequent waterflooding, the principal process was direct displacement of oil by water, resulting in additional recovery. Gas was trapped by water displacing oil that then snapped-off gas in larger pores, as in a water-wet system. However, since oil was the most wetting phase, it remained continuous in wetting and spreading layers and was not trapped by water.

We quantified saturations, interfacial areas, and curvatures during the displacement. From the total curvature, the capillary pressures could be estimated and used to interpret the displacement sequence that was observed. These results can also be linked to the four Minkowski functionals which provide a complete description of the geometry of the phases in the pore space, potentially facilitating theoretical developments (Armstrong et al., 2018; Vogel et al., 2010). Specifically, the Gaussian curvature is a measure of connectivity and can be used to quantify the degree of trapping during the displacement. A study of the principal curvatures of the gas-oil interface demonstrated the evolution of the fluid configurations as gas was injected

and later trapped. One curvature remained positive, since gas was nonwetting to oil with a positive capillary pressure, while the other changed from being negative to zero and then positive on average as the gas became less well connected.

Our results suggest that oil recovery is favored in this mixed-wet system, confirming previous work (Qin et al., 2019). However, the local displacement efficiency is less favorable than observed under near-miscible conditions (Alhosani et al., 2019). This corresponds to our traditional understanding of gas injection, where driving the gas and oil properties toward miscibility aids recovery (Lake, 1989). More surprising though is that we see significant trapping of gas during waterflooding, which is higher than in water-wet media, which is promising for storage applications. This also implies limited gas recycling is needed during EOR schemes if gas and water are both injected.

These results can serve as benchmarks to validate and calibrate pore-scale models and provide design criteria for engineering gas injection at the field scale. This work also has implications for the design of microfluidic devices where the wettability could be designed to produce fluid patterns and droplets with the desired structure and composition for a range of applications from food manufacture to drug delivery (Chen et al., 2019).

Future work could consider a wider range of samples, with perhaps more oil-wet conditions, and different displacement sequences, including multiple water alternating gas (WAG) injection cycles to assess the cycle dependency of gas trapping. We could apply this analysis to nongeological materials, such as gas diffusion layers in fuel cells, membranes, catalysts, and microfluidic devices. A thorough assessment of wettability, for example, using *in situ* contact angle measurements, should always be performed before applying this analysis—which holds for mixed-wet systems—to other materials.

Data Availability Statement

Data are available on the Digital Rocks Portal (Scanziani, Blunt, et al., 2020).

Acknowledgments

We acknowledge Abu Dhabi National Oil Company (ADNOC) for financial support. We are also very grateful to Amer Alhammadi and Ahmed Selem (Imperial College London) and Christoph Rau, Shashidhara Marathe, Kaz Wanekl, and the staff of Diamond Light Source for their work during the experiments at the synchrotron facility.

References

- Adamson, A. W., & Gast, A. P. (1997). *Physical chemistry of surfaces*. New York: Wiley.
- Alhammadi, A. M., AlRatrou, A., Singh, K., Bijeljic, B., & Blunt, M. J. (2017). In situ characterization of mixed-wettability in reservoir rock at subsurface conditions. *Scientific Reports*, 7(1), 10753.
- Alhammadi, A. M., Gao, Y., Akai, T., Blunt, M. J., & Bijeljic, B. (2020). Pore-scale X-ray imaging with measurement of relative permeability, capillary pressure and oil recovery in a mixed-wet micro-porous carbonate reservoir rock. *Fuel*, 268, 117018.
- Alhosani, A., Scanziani, A., Lin, Q., Pan, Z., Bijeljic, B., & Blunt, M. J. (2019). In situ pore-scale analysis of oil recovery during three-phase near-miscible CO₂ injection in a water-wet carbonate rock. *Advances in Water Resources*, 134, 103432.
- Alhosani, A., Scanziani, A., Lin, Q., Raeini, A. Q., Bijeljic, B., & Blunt, M. J. (2020). Pore-scale mechanisms of CO₂ storage in oilfields. *Scientific Reports*, 10(1). <https://doi.org/10.1038/s41598-020-65416-z>
- Alizadeh, A. H., & Piri, M. (2014). Three-phase flow in porous media: A review of experimental studies on relative permeability. *Reviews of Geophysics*, 52, 468–521. <https://doi.org/10.1002/2013RG000433>
- AlRatrou, A., Blunt, M. J., & Bijeljic, B. (2018). Wettability in complex porous materials, the mixed-wet state, and its relationship to surface roughness. *Proceedings of the National Academy of Sciences of the United States of America*, 115(36), 8901–8906.
- AlRatrou, A., Raeini, A. Q., Bijeljic, B., & Blunt, M. J. (2017). Automatic measurement of contact angle in pore-space images. *Advances in Water Resources*, 109, 158–169.
- Amaechi, B., Iglesias, S., Pentland, C. H., Bijeljic, B., & Blunt, M. J. (2014). An experimental study of three-phase trapping in sand packs. *Transport in Porous Media*, 103(3), 421–436.
- Ampomah, W., Balch, R. S., Cather, M., Will, R., Gunda, D., Dai, Z., & Soltanian, M. R. (2017). Optimum design of CO₂ storage and oil recovery under geological uncertainty. *Applied Energy*, 195, 80–92.
- Andrew, M. G., Bijeljic, B., & Blunt, M. J. (2014). Pore-scale contact angle measurements at reservoir conditions using X-ray microtomography. *Advances in Water Resources*, 68, 24–31.
- Andrew, M. G., Menke, H., Blunt, M. J., & Bijeljic, B. (2015). The imaging of dynamic multiphase fluid flow using synchrotron-based X-ray microtomography at reservoir conditions. *Transport in Porous Media*, 110(1), 1–24. <https://doi.org/10.1007/s11242-015-0553-2>
- Arganda-Carreras, I., Kaynig, V., Rueden, C., Eliceiri, K. W., Schindelin, J., Cardona, A., & Seung, H. S. (2017). Trainable Weka segmentation: A machine learning tool for microscopy pixel classification. *Bioinformatics*, 33(15), 2424–2426.
- Armstrong, R. T., & Berg, S. (2013). Interfacial velocities and capillary pressure gradients during Haines jumps. *Physical Review E - Statistical, Nonlinear, and Soft Matter Physics*, 88(4), 043010.
- Armstrong, R. T., McClure, J. E., Robins, V., Liu, Z., Arns, C. H., Schlüter, S., & Berg, S. (2018). Porous media characterization using Minkowski functionals: Theories, applications and future directions. *Transport in Porous Media*, 130, 305–335. <https://doi.org/10.1007/s11242-018-1201-4>
- Armstrong, R. T., McClure, J. E., Robins, V., Liu, Z., Arns, C. H., Schlüter, S., & Berg, S. (2019). Porous media characterization using Minkowski functionals: Theories, applications and future directions. *Transport in Porous Media*, 130(1), 305–335.
- Armstrong, R. T., Porter, M. L., & Wildenschild, D. (2012). Linking pore-scale interfacial curvature to column-scale capillary pressure. *Advances in Water Resources*, 46, 55–62. <https://doi.org/10.1016/j.advwatres.2012.05.009>

- Bartell, F. E., & Osterhof, H. J. (1927). Determination of the wettability of a solid by a liquid. *Industrial & Engineering Chemistry*, 19(11), 1277–1280. <https://doi.org/10.1021/ie50215a026>
- Bellamy, R., & Geden, O. (2019). Govern CO₂ removal from the ground up, 12(11), 874–876.
- Berg, S., Ott, H., Klapp, S. A., Schwing, A., Neiteler, R., Brussee, N., et al. (2013). Real-time 3D imaging of Haines jumps in porous media flow. *Proceedings of the National Academy of Sciences of the United States of America*, 110(10), 3755–3759.
- Bickle, M. J. (2009). Geological carbon storage. *Nature Geoscience*, 2(12), 815–818.
- Blunt, M. J. (2017). *Multiphase flow in permeable media: A pore-scale perspective*. Cambridge, UK: Cambridge University Press. Retrieved from <https://www.cambridge.org/it/academic/subjects/earth-and-environmental-science/applied-geoscience-petroleum-and-mining-geoscience/multiphase-flow-permeable-media-pore-scale-perspective?format=HB&isbn=9781107093461>
- Blunt, M. J., Lin, Q., Akai, T., & Bijeljic, B. (2019). A thermodynamically consistent characterization of wettability in porous media using high-resolution imaging. *Journal of Colloid and Interface Science*, 552, 59–65.
- Brown, K., Schlüter, S., Sheppard, A., & Wildenschild, D. (2014). On the challenges of measuring interfacial characteristics of three-phase fluid flow with X-ray microtomography. *Journal of Microscopy*, 253(3), 171–182.
- Buades, A., Coll, B., & Morel, J. M. (2008). Nonlocal image and movie denoising. *International Journal of Computer Vision*, 76(2), 123–139. <https://doi.org/10.1007/s11263-007-0052-1>
- Bultreys, T., & Boever, W., & Cnudde, V. (2016). Imaging and image-based fluid transport modeling at the pore scale in geological materials: A practical introduction to the current state-of-the-art. *Earth-Science Reviews*, 155, 93–128.
- Bultreys, T., Lin, Q., Gao, Y., Raeini, A. Q., AlRatrou, A., Bijeljic, B., & Blunt, M. J. (2018). Validating model predictions of pore-scale fluid distributions during two-phase flow in rocks. *Physical Review E*, 97, 053104.
- Chen, Z., Xu, J., & Wang, Y. (2019). Gas-liquid-liquid multiphase flow in microfluidic systems A review. *Chemical Engineering Science*, 202, 1–14.
- Feali, M., Pinczewski, W. V., Cinar, Y., Arns, C. H., Arns, J., South, N., & Turner, M. (2012). Qualitative and quantitative analyses of the three-phase distribution of oil , water, and gas in Bentheimer sandstone by use of micro-CT imaging. *SPE Reservoir Evaluation and Engineering*, 15, 706–711.
- Fenwick, D. H., & Blunt, M. J. (1998). Three-dimensional modeling of three phase imbibition and drainage. *Advances in Water Resources*, 21(2), 121–143.
- Ferrara, K. W., Borden, M. A., & Zhang, H. (2009). Lipid-shelled vehicles: Engineering for ultrasound molecular imaging and drug delivery. *Accounts of Chemical Research*, 42(7), 881–892.
- Garfi, G., John, C. M., Berg, S., & Krevor, S. (2020). The sensitivity of estimates of multiphase fluid and solid properties of porous rocks to image processing. *Transport in Porous Media*, 131(3), 985–1005.
- Garfi, G., John, C. M., Lin, Q., Berg, S., & Krevor, S. (2020). Fluid surface coverage showing the controls of rock mineralogy on the wetting state. *Geophysical Research Letters*, 47, e2019GL086380. <https://doi.org/10.1029/2019GL086380>
- Georgiadis, A., Llorell, F., Bismarck, A., Blas, F. J., Galindo, A., Maitland, G. C., et al. (2010). Interfacial tension measurements and modelling of (carbon dioxide + n-alkane) and (carbon dioxide + water) binary mixtures at elevated pressures and temperatures. *Journal of Supercritical Fluids*, 55(2), 743–754.
- Hildebrand, T., & Ruegsegger, P. (1997). A new method for the model-independent assessment of thickness in three-dimensional images. *Journal of Microscopy*, 185(1), 67–75. <https://doi.org/10.1046/j.1365-2818.1997.1340694.x>
- Hirasaki, G. J. (1993). Structural interactions in the wetting and spreading of van der Waals fluids. *Journal of Adhesion Science and Technology*, 7(3), 285–322.
- Hui, M. H., & Blunt, M. J. (2000). Effects of wettability on three-phase flow in porous media. *Journal of Physical Chemistry B*, 104(16), 3833–3845.
- Jones, A. C., Arns, C. H., Sheppard, A. P., Hutmacher, D. W., Milthorpe, B. K., & Knackstedt, M. A. (2007). Assessment of bone ingrowth into porous biomaterials using micro-CT. *Biomaterials*, 28(15), 2491–2504.
- Khishvand, M., Alizadeh, A. H., & Piri, M. (2016). In-situ characterization of wettability and pore-scale displacements during two- and three-phase flow in natural porous media. *Advances in Water Resources*, 97(11), 279–298.
- Kovscek, A. R., Wong, H., & Radke, C. J. (1993). A pore-level scenario for the development of mixed wettability in oil reservoirs. *AICHE Journal*, 39(6), 1072–1085. <https://doi.org/10.1002/aic.690390616>
- Kundu, A., Dumont, E., Duquenne, A.-M., & Delmas, H. (2008). Mass transfer characteristics in gas-liquid-liquid system. *The Canadian Journal of Chemical Engineering*, 81(3–4), 640–646.
- Lake, L. W. (1989). *Enhanced oil recovery*. Englewood Cliffs, NJ: Prentice Hall.
- Laplace, P. S., & Fournier, J. J. F. (1805). Sur l'action capillaire. Supplément à la théorie de l'action capillaire. *Traité de mécanique céleste*, 4(Supplement 1), 771–777.
- Lehmann, P., Berchtold, M., Ahrenholz, B., Tölke, J., Kaestner, A., Krafczyk, M., et al. (2008). Impact of geometrical properties on permeability and fluid phase distribution in porous media. *Advances in Water Resources*, 31(9), 1188–1204.
- Li, X., Boek, E., Maitland, G. C., & Trusler, J. P. M. (2012). Interfacial tension of (Brines + CO₂): (0.864 NaCl + 0.136 KCl) at temperatures between (298 and 448) K, pressures between (2 and 50) MPa, and total molalities of (1 to 5) mol · kg⁻¹. *Journal of Chemical and Engineering Data*, 57(4), 1078–1088.
- Lin, Q., Bijeljic, B., Berg, S., Pini, R., Blunt, M. J., & Krevor, S. (2019). Minimal surfaces in porous media: Pore-scale imaging of multiphase flow in an altered-wettability Bentheimer sandstone. *Physical Review E*, 99(6), 063105.
- Lin, Q., Bijeljic, B., Krevor, S. C., Blunt, M. J., Rucker, M., Berg, S., et al. (2019). A new waterflood initialization protocol with wettability alteration for pore-scale multiphase flow experiments. In *Petrophysics* (Vol. 60, pp. 264–272). Houston, TX: Society of Petrophysicists and Well-Log Analysts.
- Lin, Q., Bijeljic, B., Pini, R., Blunt, M. J., & Krevor, S. (2018). Imaging and measurement of pore-scale interfacial curvature to determine capillary pressure simultaneously with relative permeability. *Water Resources Research*, 54, 7046–7060. <https://doi.org/10.1029/2018WR023214>
- Liu, Z., Herring, A., Arns, C., Berg, S., & Armstrong, R. T. (2017). Pore-scale characterization of two-phase flow using integral geometry. *Transport in Porous Media*, 118(1), 99–117. <https://doi.org/10.1007/s11242-017-0849-5>
- Marathe, S., Storm, M., Kuppilli, V. S. C., Harrison, R., Das, G., Schroeder, S. L. M., et al. (2019). Development of synchrotron pink beam X-ray grating interferometer at the Diamond Light source I13-2 beamline. In B. Müller & G. Wang (Eds.), *Developments in X-ray tomography XII* (Vol. 11113, pp. 42). San Diego, CA: SPIE.
- Mecke, K. R., & Stoyan, D. (2000). Statistical physics and spatial statistics. In K. R. Mecke & D. Stoyan (Eds.), *Lecture Notes in Physics* (Vol. 554). Berlin, Heidelberg: Springer. <https://doi.org/10.1007/3-540-45043-2>

- Morrow, N. R. (1990). Wettability and its effect on oil recovery. *Journal of Petroleum Technology*, 42(12), 1476–1484. <https://doi.org/10.2118/21621-PA>
- National Institute of Standards and Technology (2018). In P. J. Linstrom & W. G. Mallard (Eds.), *NIST Chemistry WebBook*.
- Øren, P. E., Billiotte, J., & Pinczewski, W. V. (1992). Mobilization of waterflood residual oil by gas injection for water-wet conditions. *SPE Formation Evaluation*, 7, 70–78.
- Pak, T., Butler, I. B., Geiger, S., van Dijke, M. I. J., & Sorbie, K. S. (2015). Droplet fragmentation: 3D imaging of a previously unidentified pore-scale process during multiphase flow in porous media. *Proceedings of the National Academy of Sciences of the United States of America*, 112(7), 1947–52.
- Piri, M., & Blunt, M. J. (2005). Three-dimensional mixed-wet random pore-scale network modeling of two- and three-phase flow in porous media. I. Model description. *Physical Review E - Statistical, Nonlinear, and Soft Matter Physics*, 71(2), 026301. <https://doi.org/10.1103/PhysRevE.71.026301>
- Qin, Z., Arshadi, M., & Piri, M. (2019). Micro-scale experimental investigations of multiphase flow in oil-wet carbonates. II. Tertiary gas injection and WAG. *Fuel*, 257, 116012.
- Raeini, A. Q., Bijeljic, B., & Blunt, M. J. (2018). Generalized network modeling of capillary-dominated two-phase flow. *Physical Review E*, 97, 23308.
- Rau, C., Storm, M., Marathe, S., Bodey, A. J., Zdora, M.-C., Cipiccia, S., et al. (2019). Fast multi-scale imaging using the Beamline I13L at the Diamond Light Source. In B. Müller & G. Wang (Eds.), *Developments in X-ray tomography XII* (Vol. 11113, pp. 68). San Diego, CA: SPIE. <https://doi.org/10.1117/12.2543405.full>
- Reynolds, C. A., Andrew, M. G., Menke, H., Krevor, S., & Blunt, M. J. (2017). Dynamic fluid connectivity during steady-state multiphase flow in a sandstone. *Proceedings of the National Academy of Sciences*, 114(31), 8187–8192.
- Rücker, M., Bartels, W. B., Singh, K., Brussee, N., Coorn, A., van der Linde, H. A., et al. (2019). The effect of mixed wettability on pore-scale flow regimes based on a flooding experiment in Ketton limestone. *Geophysical Research Letters*, 46, 3225–3234. <https://doi.org/10.1029/2018GL081784>
- Scanziani, A., Blunt, M., Bijeljic, B., Garfi, G., Lin, Q., & Alhammadi, A. (2020). Dynamics of immiscible three-phase flow in a mixed-wet Ketton limestone sample. <http://www.digitalrockspotal.org/projects/253>
- Scanziani, A., Lin, Q., Alhosani, A., Blunt, M. J., & Bijeljic, B. (2020). Dynamics of fluid displacement in mixed-wet porous media. *Proceedings of the Royal Society A: Mathematical, Physical and Engineering Sciences*, 476(2240), 20200040. <https://doi.org/10.1098/rspa.2020.0040>
- Scanziani, A., Singh, K., Blunt, M. J., & Guadagnini, A. (2017). Automatic method for estimation of in situ effective contact angle from X-ray micro tomography images of two-phase flow in porous media. *Journal of Colloid And Interface Science*, 496, 51–59. <https://doi.org/10.1016/j.jcis.2017.02.005>
- Scanziani, A., Singh, K., Bultreys, T., Bijeljic, B., & Blunt, M. J. (2018). In situ characterization of immiscible three-phase flow at the pore scale for a water-wet carbonate rock. *Advances in Water Resources*, 121, 446–455.
- Scanziani, A., Singh, K., Menke, H., Bijeljic, B., & Blunt, M. J. (2020). Dynamics of enhanced gas trapping applied to CO₂ storage in the presence of oil using synchrotron X-ray micro tomography. *Applied Energy*, 259, 114136.
- Schlüter, S., Sheppard, A., Brown, K., & Wildenschild, D. (2014). Image processing of multiphase images obtained via X-ray microtomography: A review. *Water Resources Research*, 50, 3615–3639. <https://doi.org/10.1002/2014WR015256>
- Scott, V., Haszeldine, R. S., Tett, S. F. B., & Oschlies, A. (2015). Fossil fuels in a trillion tonne world. *Nature Climate Change*, 5(5), 419–423.
- Singh, K., Bijeljic, B., & Blunt, M. J. (2016). Imaging of oil layers, curvature and contact angle in a mixed-wet and a water-wet carbonate rock. *Water Resources Research*, 52, 1716–1728. <https://doi.org/10.1002/2015WR018072>
- Singh, K., Menke, H., Andrew, M., Lin, Q., Rau, C., Blunt, M. J., & Bijeljic, B. (2017). Dynamics of snap-off and pore-filling events during two-phase fluid flow in permeable media. *Scientific Reports*, 7(1), 5192.
- Sohrabi, M., Danesh, A., Tehrani, D. H., & Jamialahmady, M. (2008). Microscopic mechanisms of oil recovery by near-miscible gas injection. *Transport in Porous Media*, 72(3), 351–367.
- Szulcowski, M. L., MacMinn, C. W., Herzog, H. J., & Juanes, R. (2012). Lifetime of carbon capture and storage as a climate-change mitigation technology. *Proceedings of the National Academy of Sciences of the United States of America*, 109(14), 5185–5189.
- Van Dijke, M. I. J., & Sorbie, K. S. (2002). Pore-scale network model for three-phase flow in mixed-wet porous media. *Physical Review E*, 66, 046302. <https://doi.org/10.1103/PhysRevE.66.046302>
- Van Dijke, M. I. J., & Sorbie, K. S. (2003). Three-phase capillary entry conditions in pores of noncircular cross-section. *Journal of Colloid and Interface Science*, 260, 385–397.
- Van Dijke, M. I. J., Sorbie, K. S., Sohrabi, M., & Danesh, A. (2006). Simulation of WAG floods in an oil-wet micromodel using a 2-D pore-scale network model. *Journal of Petroleum Science and Engineering*, 52, 71–86.
- Vogel, H.-J., Weller, U., & Schlüter, S. (2010). Quantification of soil structure based on Minkowski functions. *Computers & Geosciences*, 36(10), 1236–1245.
- Wildenschild, D., Armstrong, R. T., Herring, A. L., Young, I. M., & Carey, J. W. (2011). Exploring capillary trapping efficiency as a function of interfacial tension, viscosity, and flow rate. *Energy Procedia*, 4, 4945–4952.
- Wildenschild, D., Hopmans, J. W., Rivers, M. L., & Kent, A. J. R. (2005). Quantitative analysis of flow processes in a sand using synchrotron-based X-ray microtomography. *Vadose Zone Journal*, 4(1), 112–126.
- Wildenschild, D., & Sheppard, A. (2013). X-ray imaging and analysis techniques for quantifying pore-scale structure and processes in subsurface porous medium systems. *Advances in Water Resources*, 51, 217–246.
- Zúñiga, R. N., & Aguilera, J. M. (2008). Aerated food gels: Fabrication and potential applications. *Trends in Food Science and Technology*, 19(4), 176–187.